A Diagnostic Study of Waves on the Tropopause

YOSHIHIRO TOMIKAWA AND KAORU SATO*

National Institute of Polar Research, Tokyo, Japan

THEODORE G. SHEPHERD

Department of Physics, University of Toronto, Toronto, Ontario, Canada

(Manuscript received 15 June 2005, in final form 11 February 2006)

ABSTRACT

The spatial structure and phase velocity of tropopause disturbances localized around the subpolar jet in the Southern Hemisphere are investigated using 6-hourly European Centre for Medium-Range Weather Forecasts reanalysis data covering 15 yr (1979–93). The phase velocity and phase structure of the tropopause disturbances are in good agreement with those of an edge wave vertically trapped at the tropopause. However, the vertical distribution of the ratio of potential to kinetic energy exhibits maxima above and below the tropopause and a minimum around the tropopause, in contradiction to edge wave theory for which the ratio is unity throughout the troposphere and stratosphere. This difference in vertical structure between the observed tropopause disturbances and edge wave theory is attributed to the effects of a finite-depth tropopause together with the next-order corrections in Rossby number to quasigeostrophic dynamics.

1. Introduction

Cyclonic tropopause disturbances observed in the extratropics have been extensively studied because they play a primary role in type-B cyclogenesis (Petterssen and Smebye 1971) and are often accompanied by jet streaks (Pyle et al. 2004). However, their anticyclonic counterparts have not attracted much attention because their amplitudes are much smaller than those of the cyclonic disturbances (Hakim and Canavan 2005). While the cyclonic disturbances have closed contours of geopotential or relative vorticity in the midtroposphere, and of potential temperature at the tropopause, the corresponding contours associated with the anticyclonic disturbances are wavelike (Hakim 2000). Because of this cyclone–anticyclone asymmetry, cyclonic tropopause disturbances have usually been identified as isolated vortexlike structures and studied by tracking extrema of geopotential (Sanders 1988) or vorticity-related quantities (Lefevre and Nielsen-Gammon 1995) at 500 hPa, and of potential temperature at the dynamical tropopause (Pyle et al. 2004). These observational studies showed that cyclonic tropopause disturbances in the Northern Hemisphere (NH) are most frequently observed in the northwesterly or southwesterly flow of the jet stream, and have a mean lifetime of 5 days. To explain their isolated vortexlike structure, monopolar and dipolar vortices with a strong nonlinearity of $O(1)$ or larger embedded in the jet stream have been suggested as conceptual models (Cunningham and Keyser 2000, 2004; Hakim 2000). These models successfully reproduce the isolated structure and jet streaks associated with the cyclonic disturbances. However, they do not provide any constraint on the vertical structure of the tropopause disturbances, because either a barotropic model is employed or the vertical structure is explicitly given in their studies.

On the other hand, tropopause disturbances often have a wavelike structure, and some studies have therefore treated tropopause disturbances as waves. Rivest et al. (1992) showed that a vertically unbounded quasigeostrophic Eady model with a piecewise constant potential vorticity in both the troposphere and stratosphere had an edge wave solution at the tropopause

* Current affiliation: Department of Earth and Planetary Science, The University of Tokyo, Tokyo, Japan.

Corresponding author address: Dr. Yoshihiro Tomikawa, Polar Meteorology and Glaciology Group, National Institute of Polar Research, 1-9-10 Kaga, Itabashi-ku, Tokyo 173-8515, Japan.
E-mail: tomikawa@nipr.ac.jp

(see also Juckes 1994). Muraki and Hakim (2001) took into account the next-order corrections in Rossby number to quasigeostrophic dynamics and showed that the edge wave solution acquired a cyclone–anticyclone asymmetry similar to that of observed tropopause disturbances. Observational studies of tropopause disturbances from a wave perspective (Sato et al. 1993; Hirota et al. 1995; Yamamori et al. 1997) have shown that these tropopause disturbances have zonal wavelengths of 2000–3000 km and periods of 20–30 h, and are localized around the tropopause slightly poleward of the subpolar or polar front jet in the NH, where the latitudinal gradients of potential vorticity are maximized. Sato et al. (2000) also showed that tropopause disturbances exist around the Southern Hemisphere (SH) subpolar jet.

In this paper, we examine the extent to which observed tropopause disturbances may be interpreted within the context of the edge wave theory of Rivest et al. (1992). After the description of the data and the filter in section 2, the distributions of phase velocity, phase structure, and potential energy and kinetic energy, and the ratio of potential to kinetic energy for the tropopause disturbances are given in section 3. An inconsistency between observed tropopause disturbances and the edge wave solution of Rivest et al. (1992) is demonstrated from the vertical distribution of the ratio of potential to kinetic energy. In section 4, the effects of a finite-depth tropopause and the next-order corrections in Rossby number on the edge wave solution are discussed. A summary and concluding remarks are given in section 5.

2. Data and filter

Our analysis is based on the European Centre for Medium-Range Weather Forecasts (ECMWF) Re-Analysis basic level III data with a time interval of 6 h (0000, 0600, 1200, and 1800 UTC) (Gibson et al. 1997). The data are distributed on a 2.5° latitude × 2.5° longitude grid at 17 pressure levels (1000, 925, 850, 775, 700, 600, 500, 400, 300, 250, 200, 150, 100, 70, 50, 30, and 10 hPa). The dataset covers 15 yr from 1 January 1979 through 31 December 1993.

Tropopause wavelike disturbances have ground-based wave periods of 20–30 h (Sato et al. 1993; Hirota et al. 1995; Yamamori et al. 1997). Thus, in order to isolate the disturbances, a high-pass filter with a cutoff period of 48 h is applied to the time series data. Figure 1 shows the response function of the high-pass filter. This filter extracts the disturbances with a wave period of 12–48 h when aliasing from higher-frequency motions is negligible. Aliasing turns out to be insignificant

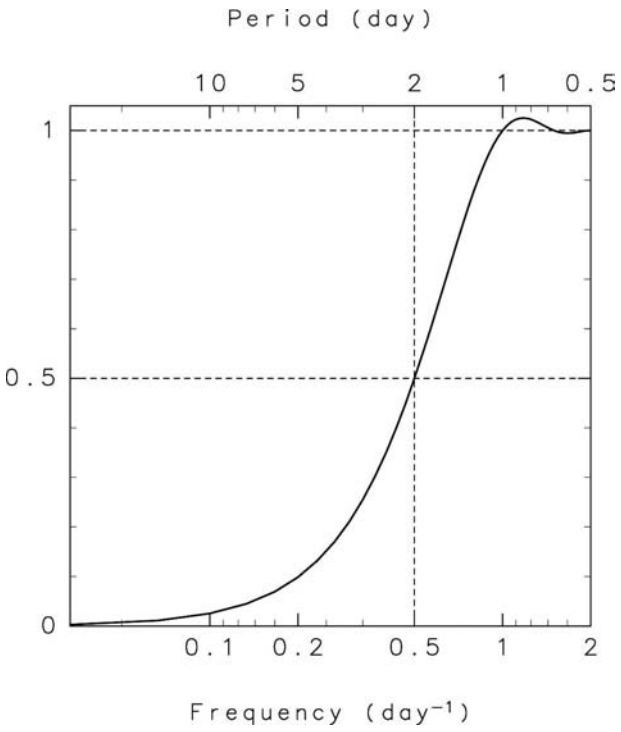

FIG. 1. Response function of high-pass filter used to extract the short-period (<48 h) disturbances.

because westward-propagating disturbances are not observed in this analysis (i.e., if aliasing would occur, eastward-propagating disturbances would be observed as westward-propagating disturbances). A potential deficiency of such a filter is that it may change the structure of a wave packet by increasing its zonal extent (Wallace et al. 1988; Berbery and Vera 1996). Figures 2a and 2b show one-point correlation maps of unfiltered and high-pass-filtered meridional winds at 300 hPa at 0000 UTC 9 August 1990. While the high-pass-filtered data successfully extract the tropopause disturbances with a zonal wavelength of about 2500 km, the wave packets in high-pass-filtered data are indeed more zonally elongated than those in the unfiltered data. However, because the phase velocity and spatial structure of the tropopause disturbances discussed in this paper are not significantly affected by this filter, the filtered data are suitable for the purpose of the present analysis. A zonal wavenumber–frequency spectrum of high-pass-filtered meridional wind at 50°S and 300 hPa averaged over January–December is shown in Fig. 3 in the energy content form (cf. appendix A of Horinouchi et al. 2003). Large power remains in the region with a long-wave period (>2 days) even after the high-pass filtering, because the high-pass filter has a spectral leakage in the region with a period longer than the cutoff period (= 2 days) and the isolation of spectral peaks between

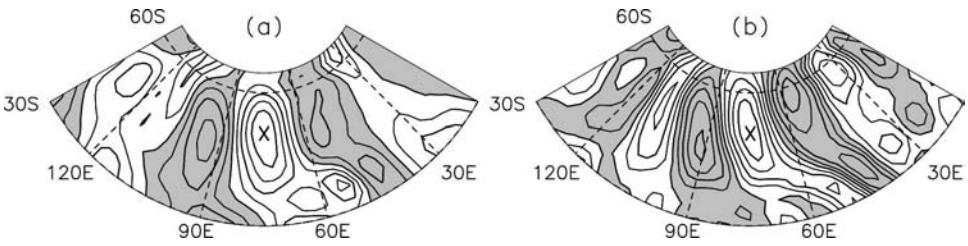

FIG. 2. One-point correlation maps of (a) unfiltered and (b) high-pass-filtered meridional winds at 300 hPa at 0000 UTC 9 Aug 1990. Contour intervals are 0.1. Negative correlation coefficients are shaded. A cross represents the base point at 50°S, 75°E.

synoptic-scale (i.e., 2–10 days) and short-period (<2 days) disturbances is not clear. However, the high-pass-filtered data exhibit many features characteristic of tropopause disturbances, which are consistent with previous studies (e.g., Hakim 2000), as shown in the following section. Furthermore, using filtered data with different cutoff periods of 36, 42, 54, and 60 h did not significantly change the results (not shown). The low-pass-filtered data with a cutoff period of 48 h are called "background" data in this paper.

3. Results

a. Horizontal distributions

Figure 4 shows a time–latitude section of zonal-mean kinetic energy [KE $\equiv \overline{(u'^2 + v'^2)}/2$, where u' and v' are high-pass-filtered components of zonal and meridional winds, respectively] of tropopause disturbances and of the latitudinal gradient of quasigeostrophic potential vorticity (QGPV) at 300 hPa. QGPV is defined as (Andrews et al. 1987)

$$q = f + \frac{1}{a\cos\phi}\frac{\partial v}{\partial \lambda} - \frac{1}{a\cos\phi}\frac{\partial}{\partial \phi}(u\cos\phi) + \frac{f}{p}\frac{R}{H_0}\frac{\partial}{\partial z}\left[\frac{p}{N^2}(T - T_0)\right] \quad (1)$$

in spherical geometry, where q is QGPV, f is the Coriolis parameter, $H_0 = 7$ km is a scale height, $z \equiv H_0 \ln(p_s/p)$ (where $p_s = 1000$ hPa) is the log pressure height, R is the gas constant, and N is the buoyancy frequency computed from T_0, which is defined as the monthly and zonal-mean temperature at 60° latitude in each hemisphere. Other notation follows standard convention. The 300-hPa pressure level is used because, as shown later, the KE of tropopause disturbances is maximized at 300 hPa (see also Sato et al. 2000). Distributions of the KE and QGPV gradient have a large difference between the SH and the NH. While the KE and QGPV gradient in the NH have weaker and broader maxima, both the KE and the QGPV gradient in the SH have clear maxima around 50°S. This is because quasi-stationary planetary waves are more active in the NH than in the SH. Because the lag correlation analysis to calculate the phase velocity of tropopause disturbances in the next subsection needs to assume zonal symmetry of the background fields, we focus on tropopause disturbances in the SH in this paper.

Figure 5 shows the horizontal distributions of the zonal wind and QGPV gradient in each month from January to December at 300 hPa. While the subpolar jet is located around 50°S throughout the year, the subtropical jet is observed only in austral winter around

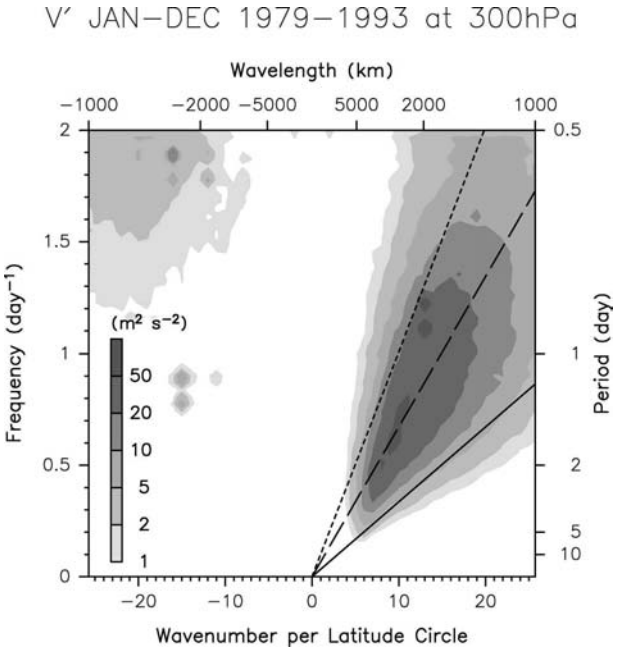

FIG. 3. Two-dimensional power spectrum of high-pass-filtered meridional wind in the energy content form as a function of zonal wavenumber per latitude circle and frequency (day^{-1}) at 50°S at 300 hPa averaged throughout the year. Positive and negative wavenumbers represent eastward and westward propagations, respectively. Top and right axes represent the zonal wavelength and ground-based wave period, respectively. Ground-based phase velocities of 10 (solid), 20 (dashed), and 30 m s^{-1} (dotted) are shown.

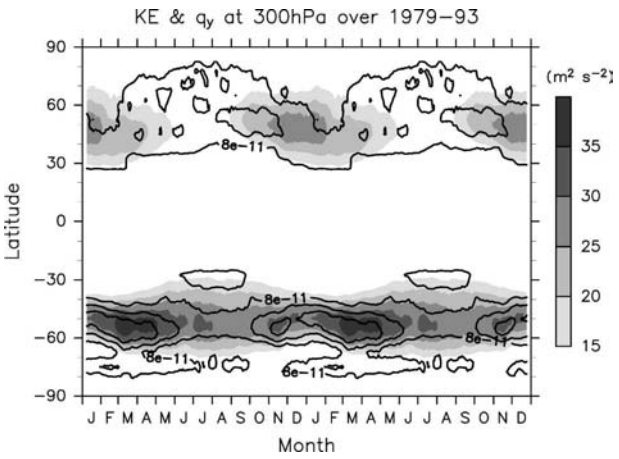

FIG. 4. Time–latitude section of zonal-mean KE (shades) and of the latitudinal gradient of QGPV (contours) at 300 hPa. Contour intervals are 4×10^{-11} m^{-1} s^{-1}. Two annual cycles are shown.

30°S. Both the subpolar and subtropical jets accompany maxima of the QGPV gradient.

Figure 6 shows the horizontal distributions of KE and the QGPV gradient in each month from January to December at 300 hPa. While the distributions of KE and the QGPV gradient accord very well around the subpolar jet, the maxima of the QGPV gradient associated with the subtropical jet do not have corresponding isolated maxima of KE. The absence of KE maxima around the subtropical jet in the SH is also reported by Sato et al. (2000).

b. Phase velocity

Figure 7 shows a scatter diagram of intrinsic phase velocity (i.e., phase velocity relative to the longitudinally averaged zonal wind) of the high-pass-filtered disturbances versus QGPV gradient averaged over the longitude region of 30°W–60°E–150°E at 50°S and 300 hPa. The longitude region of 30°W–60°E–150°E was chosen because the QGPV gradient is maximized and the tropopause disturbances are most active there (Fig. 6). The ground-based phase velocity is estimated using the longitudinally lagged cross-correlation between two longitudinal data series of high-pass-filtered meridional wind in the longitude region of 30°W–60°E–150°E with a 6-h time difference. When the maximum cross-correlation coefficient is larger than 0.7, the corresponding lag of longitude divided by 6 h is taken as the ground-based phase velocity. The intrinsic phase velocity is computed as the ground-based phase velocity minus the zonal wind averaged over the longitude region of 30°W–60°E–150°E. The data are plotted only when the longitudinally averaged QGPV gradient is maximized at 50°S and 300 hPa. The gray dashed line in Fig. 7 represents the least squares linear fit to the data when the intrinsic phase velocity and QGPV gradient are taken to be the dependent and independent variables, respectively. The intrinsic phase velocity and QGPV gradient show a clear negative correlation (i.e., the magnitude of the intrinsic phase velocity gets larger as the QGPV gradient increases), whose correlation coefficient (−0.63) is significant at the 99% confidence level.

In the edge wave solution of Rivest et al. (1992), the intrinsic phase velocity is proportional to the QGPV gradient integrated with height over the tropopause region (B6). To demonstrate a quantitative relationship between the intrinsic phase velocity of the tropopause disturbances and that of Rivest et al.'s edge wave solution, the intrinsic phase velocity of Rivest et al.'s solution is shown by the gray solid line in Fig. 7, where the QGPV gradient is integrated over a depth of 3 km, the background zonal wind at the tropopause is set to 36 m s^{-1} (see Fig. 6), and the other parameters are the same as those in Rivest et al. (1992). The intrinsic phase velocity of Rivest et al.'s solution is in good agreement with that of the tropopause disturbances shown by the gray dashed line, both qualitatively and quantitatively.

c. Phase structure

To examine the phase structure of the tropopause disturbances, longitude–pressure lag-correlation maps of high-pass-filtered geopotential, temperature, and omega velocity at 50°S are presented in Fig. 8. Longitudinal lag-correlation coefficients are averaged over the same 1284 cases as in Fig. 7. The reference point is marked by "×" for each component. The reference points for the geopotential and temperature maps are taken at 300 and 500 hPa, because the kinetic and potential energy of the tropopause disturbances are maximized at 300 and 500 hPa, respectively, as shown later. The lag-correlation map of omega velocity shows a similar structure for both the reference points at 300 and 500 hPa. The geopotential fluctuation exhibits a nearly barotropic structure and has a zonal wavelength of 2500–3000 km. The temperature fluctuation changes its sign across 300 hPa. The omega velocity fluctuation abruptly loses the correlation above 200 hPa. Note that because the lag-correlation map represents a phase structure relative to the reference point, Fig. 8 does not mean that the omega velocity is in phase with the geopotential and temperature (i.e., omega velocity is 90° out of phase with geopotential and temperature, as shown in Fig. 12). These phase structures of geopotential, temperature, and omega velocity are in good agreement with previous observational studies of tropopause disturbances [e.g., Fig. 10 of Sato et al.

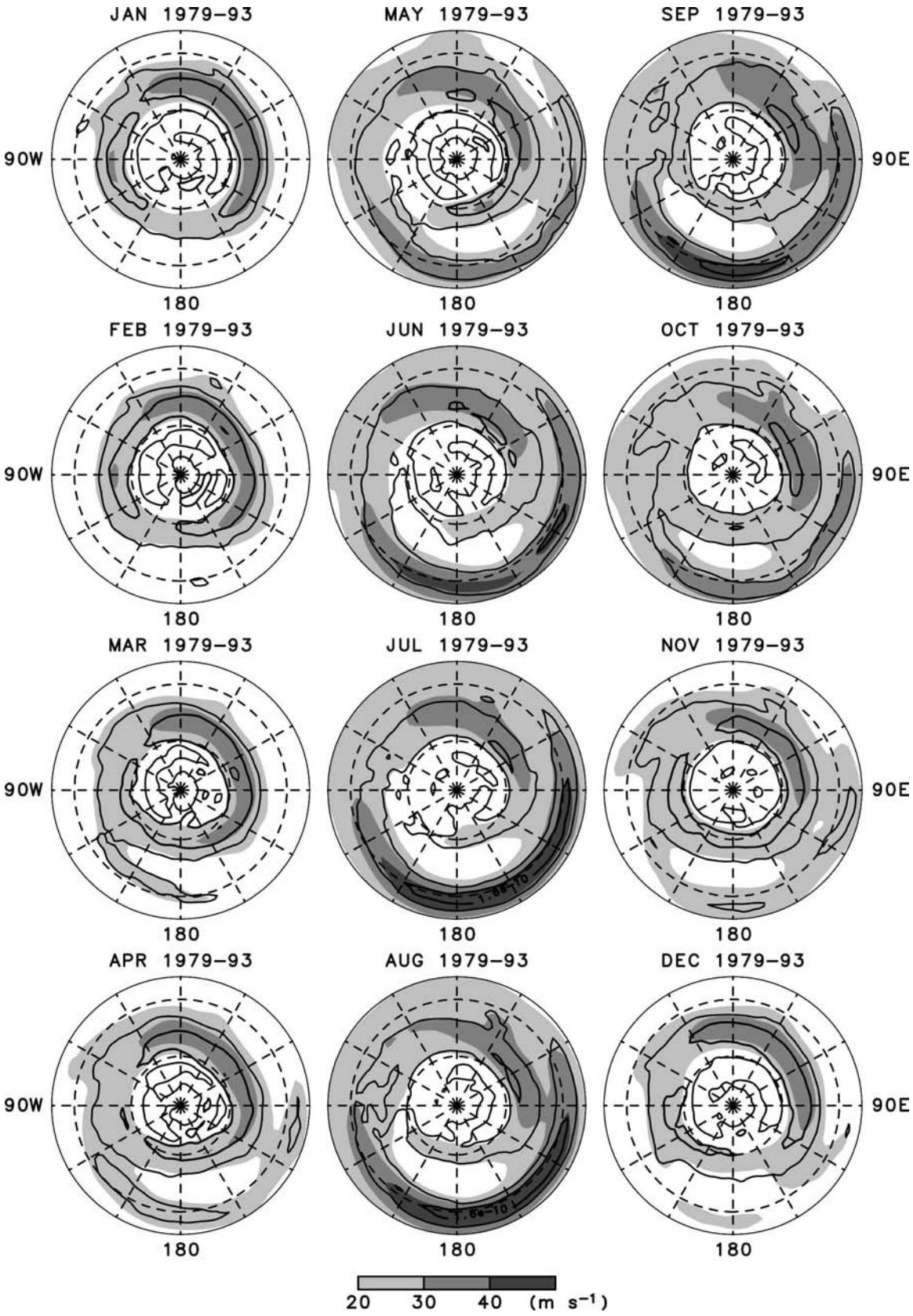

FIG. 5. Horizontal distributions of zonal wind (shades) and latitudinal gradient of QGPV (contours) at 300 hPa in the SH from January through December. Dashed circles show latitudes of 60° and 30°S. Contour intervals are 8×10^{-11} m^{-1} s^{-1}.

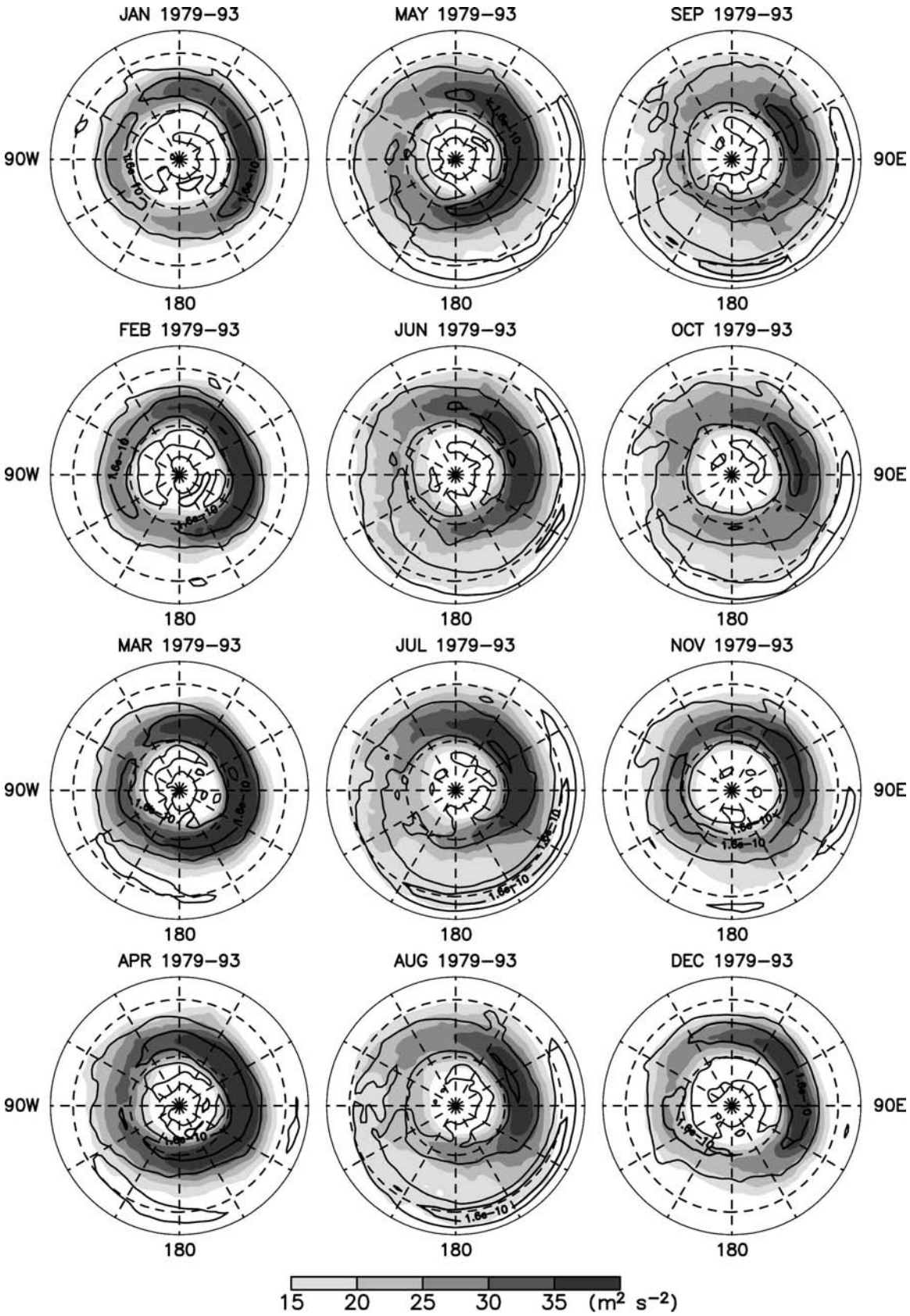

FIG. 6. The same as Fig. 5, but for KE rather than zonal wind (shades).

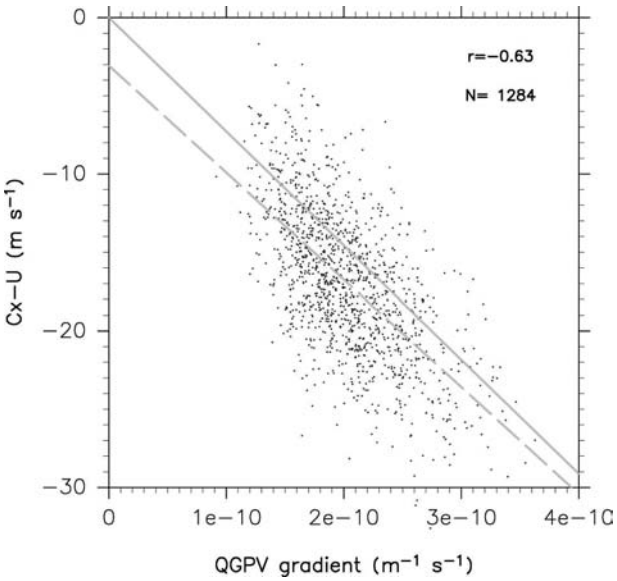

FIG. 7. Scatter diagram of intrinsic phase velocity of the high-pass-filtered disturbances vs QGPV gradient averaged over the longitude region of 30°W–60°E–150°E at 50°S and 300 hPa; (top right) r and N denote the correlation coefficient and the number of data points used for the calculation of the correlation coefficient, respectively. The gray solid and dashed lines represent the intrinsic phase velocity of the edge wave solution discussed in the text and a linear least squares fit to the data, respectively.

(1993); Fig. 10 of Hakim (2000); Fig. 9 of Hakim and Canavan (2005)]. These features are also consistent with the edge wave solution of Rivest et al. (1992), in which the fluctuations are barotropic, the temperature fluctuation changes its sign across the tropopause, and the vertical velocity is attenuated quickly in the stratosphere [e.g., Fig. 4 of Rivest et al. (1992); Figs. 12a–c herein]. The zonal wavelength of the omega velocity fluctuation looks shorter than that of the geopotential and temperature, because the omega velocity of nonmonochromatic waves weights shorter horizontal wavelengths compared to the geopotential and temperature. On the other hand, this correlation-based method cannot describe the vertical variation of the disturbance amplitude, because the correlation is inevitably larger near the reference point. In the next subsection, potential and kinetic energy, and potential-to-kinetic energy ratio are presented in order to give additional information on the vertical structure of the tropopause disturbances.

d. Vertical distributions

Figure 9 shows the vertical distributions of KE, potential energy [PE $\equiv \overline{(RT'/NH_0)^2}/2$], and PE/KE at 50°S from January to December. While the KE is maximized at 300 hPa in all months, the PE is maximized at 200 and 500 hPa. As a result, PE/KE is mostly maximized at 150–200 and 500–700 hPa and minimized at 300 hPa. Such a vertical variation of PE/KE is inconsistent with Rivest et al.'s edge wave solution, in which PE/KE is unity throughout the troposphere and the stratosphere.

Although Rivest et al. (1992) employed the Boussinesq approximation, the effect of density stratification is expected to be small because the Rossby height ($H_R \equiv f/\kappa N \approx 2$ km, where κ is a horizontal wavenumber and $2\pi/\kappa \approx 2500$ km) of edge waves is much smaller than the scale height (= 9 km) in Rivest et al.'s model. The Rossby height represents the extent of vertical penetration of an edge wave. The horizontal scale of about 2500 km is obtained by the previous observational studies from a wave perspective (Sato et al. 1993, 2000; Hirota et al. 1995; Yamamori et al. 1997) and is also used in Rivest et al. (1992).

Another feature of the observations is that the maxima of PE/KE in the troposphere (i.e., 1–1.2) are much larger than those in the stratosphere (i.e., 0.4–0.5). If the vertical scale of tropopause disturbances is defined as the e^2-folding scale of KE (i.e., the e-folding scale of streamfunction), it is estimated at about 5 km in the stratosphere. Because the vertical scale of Rivest et al.'s solution given by the Rossby height is about 2 km in the stratosphere, it is significantly smaller than the observed vertical scale. Thus, while the phase velocity and phase structure of tropopause disturbances are in good agreement with Rivest et al.'s solution, the vertical structure is clearly different.

4. Corrections to the vertical structure of edge waves

a. Finite-depth tropopause

To investigate the vertical structure of edge waves when the tropopause has a finite depth, the QGPV equation (A8) is numerically solved as an eigenvalue problem, following Rivest and Farrell (1992) and Farrell (1982). When the latitudinal variation of the Coriolis parameter is set to zero (i.e., f-plane approximation), the QGPV equation has a neutral solution localized at the tropopause (see Fig. 16 of Rivest and Farrell 1992) corresponding to the edge wave solution in Rivest et al. (1992). Figure 10 shows the zonal cross sections of nondimensional streamfunction, potential temperature, and vertical velocity of the neutral solution under the same background flow and parameter settings as those of Rivest and Farrell (1992). All of the variables are nondimensionalized. Descriptions of background flow and parameter settings are given in appendix A. The tropopause defined by the maximum of QGPV gradi-

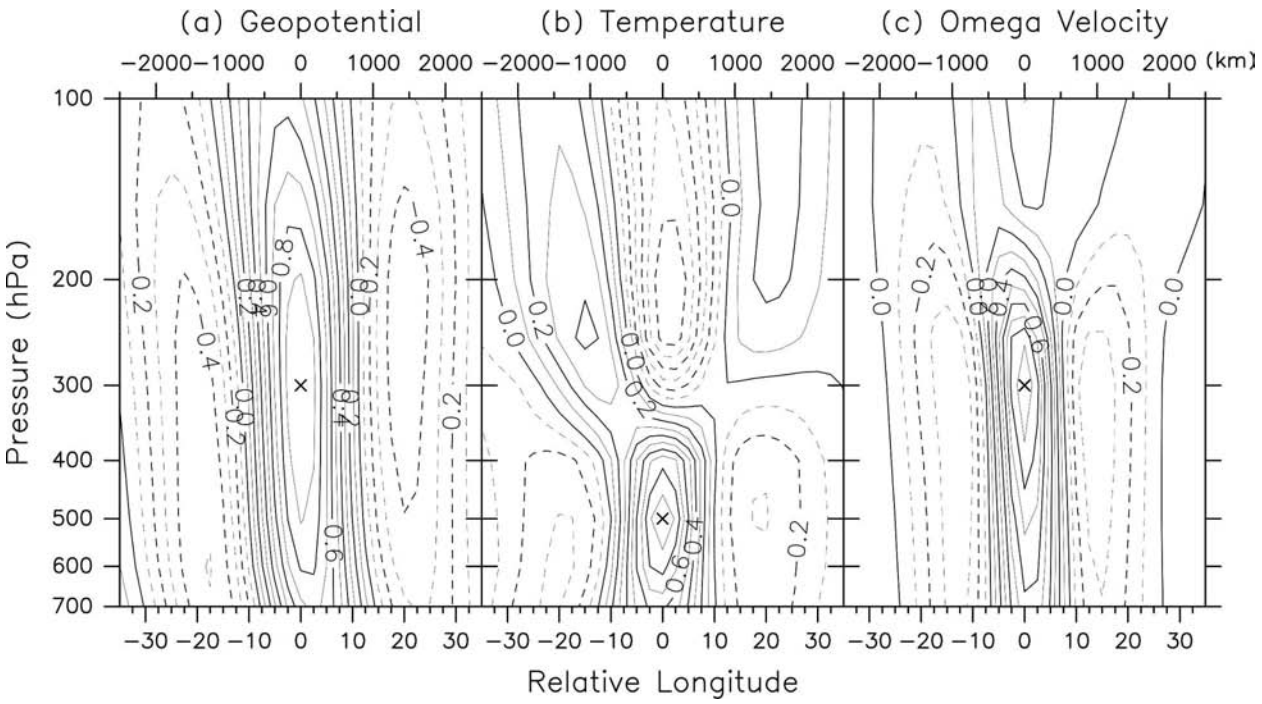

FIG. 8. Longitude–pressure lag-correlation diagrams of high-pass-filtered (a) geopotential, (b) temperature, and (c) omega velocity at 50°S averaged over the same cases as plotted in Fig. 7. Crosses represent the reference points. Contour intervals are 0.1. Top axis represents a horizontal distance.

ent is located around $z = 0.96$. The potential temperature anomaly is continuous at the tropopause unlike Rivest et al.'s edge wave solution, and is maximized above and below the tropopause. The streamfunction and vertical velocity anomalies have a structure similar to that of Rivest et al.'s solution (see Figs. 12a–c). These vertical structures are explained in terms of the inversion of a finite-depth QGPV anomaly (Hoskins et al. 1985). Because the static stability anomaly has the same (opposite) sign as the QGPV anomaly inside (outside) the QGPV anomaly, the potential temperature anomaly is maximized at the top and bottom of the finite-depth QGPV anomaly. On the other hand, the streamfunction (and horizontal wind) anomaly is maximized at the height of the QGPV anomaly center. It is worth noting that the streamfunction of the neutral solution asymptotically approaches that of Rivest et al.'s edge wave solution in the limit of a zero-depth tropopause [i.e., δ_u and $\delta_N \to 0$ in (A12) and (A13), respectively] under the Boussinesq approximation (i.e., $s = 0$ in appendix A). The intrinsic phase velocity of the neutral solution is hardly changed by the finite-depth tropopause.

Figure 11 shows the vertical distributions of KE, PE, and PE/KE of the neutral solution. While the KE is maximized at the tropopause, the PE is maximized above and below the tropopause and minimized at the tropopause. Also, PE/KE is maximized above and below the tropopause (PE/KE $\approx$ 0.8 and 1.1, respectively) and minimized at the tropopause (PE/KE = 0). These vertical distributions of KE, PE, and PE/KE reproduce the observed structure shown in Fig. 9 quite well both qualitatively and quantitatively, although a few differences from the observations remain. The PE/KE ratio in the stratosphere does not show as well-defined maxima as do the observations in austral winter. This is probably because the short-period disturbances localized around the stratospheric winter polar vortex (Tomikawa and Sato 2003) have a small PE/KE and largely contaminate the PE/KE ratio in the middle stratosphere during this period. In contrast, the observed PE/KE distributions in the stratosphere are almost flat in austral summer (Fig. 9), as in the neutral solution. However, two discrepancies still remain. First, the difference in PE/KE maxima between the troposphere and stratosphere are not so large in Fig. 11 as in the observations. Second, the dimensional vertical scale estimated from Fig. 11 is 2–3 km and still smaller than the observed value. These issues are discussed in the next subsection.

b. Next-order corrections in Rossby number

Muraki et al. (1999) expressed the next-order corrections in Rossby number (ϵ) to quasigeostrophic dynam-

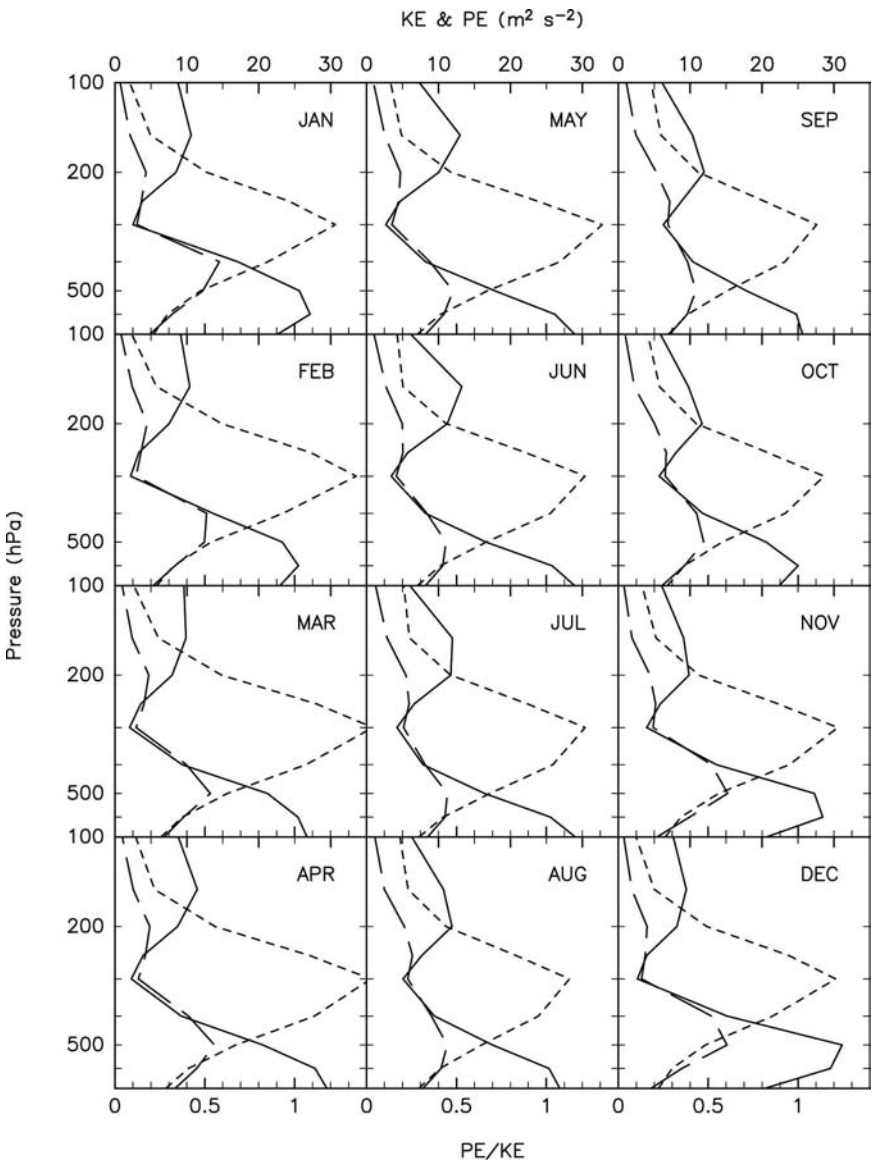

FIG. 9. Vertical distributions of KE (short dashed), PE (long dashed), and PE/KE (solid) at 50°S in each month of January through December.

ics by representing primitive variables (v, $-u$, θ) in terms of scalar and vector potentials (i.e., Helmholtz decomposition). Muraki and Hakim (2001) applied this method to the edge wave solution at the tropopause and successfully reproduced the cyclone–anticyclone asymmetry of tropopause disturbances. Figure 12 shows the zonal cross sections of nondimensional streamfunction, dimensional potential temperature, and vertical velocity of the edge wave solutions without and with the next-order corrections in Rossby number (hereafter, referred to as QG and QG^{+1} solutions, respectively), where $k = 2.3$ and $l = 1.4$ are nondimensional zonal and meridional wavenumbers, respectively, $\epsilon A = 0.03$, A is a nondimensional amplitude of streamfunction, and descriptions of the background flow and other parameter settings are given in appendix B. A dimensional zonal wavelength corresponding to $k = 2.3$ is 2500 km. To treat a realistic tropopause with a cyclone–anticyclone asymmetry, $\epsilon A = 0.03$ is used here. When ϵA is smaller (larger) than 0.03, the tropopause of the QG^{+1} solution gets bulged (dented) at its anticyclonic center. The tropopause height is maximized at the anticyclonic center in the actual atmosphere. On the other hand, the cyclone–anticyclone asymmetry of the QG^{+1} solution comes from the nonlinear parts of the next-order corrections (Muraki and Hakim 2001).

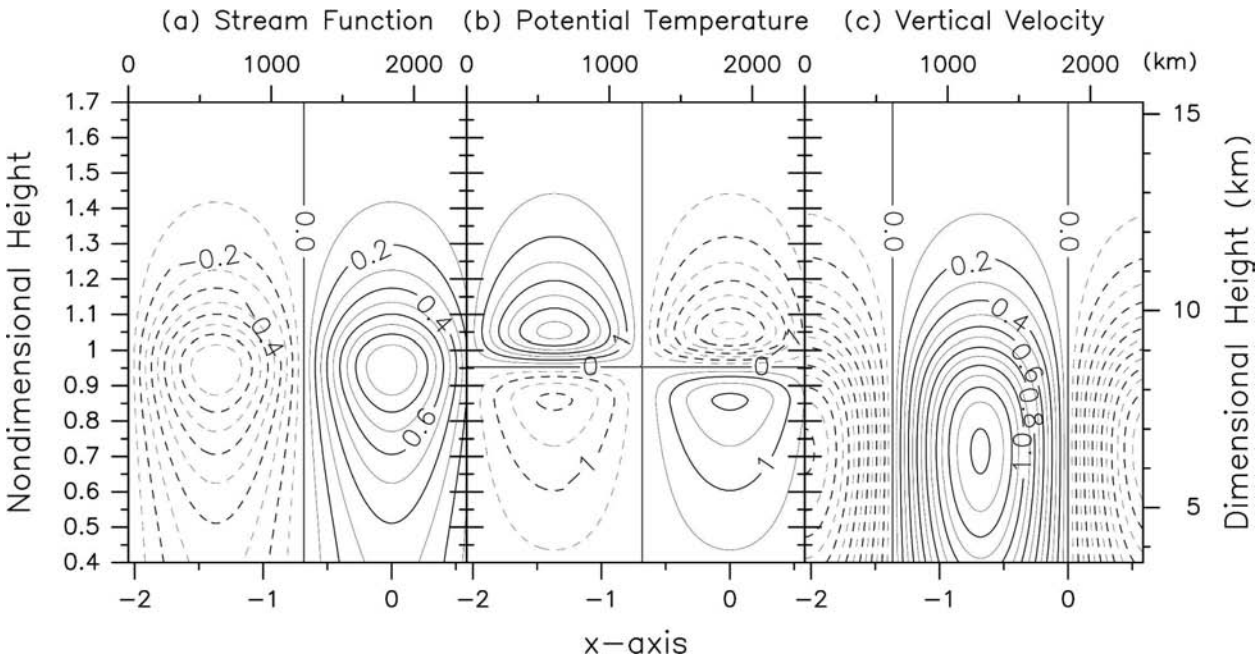

FIG. 10. Zonal cross sections of nondimensional (a) streamfunction, (b) potential temperature, and (c) vertical velocity of the neutral solution. Contour intervals are 0.1 in (a) and (c), and 0.5 in (b). Dashed contours represent negative values. Top axis represents a horizontal distance.

Because the amplitude of the nonlinear parts is proportional to $(\epsilon A)^2$, ϵA needs to be large for the cyclone–anticyclone asymmetry to appear. When the Coriolis parameter (f) and the horizontal scale (L) are fixed, dimensional amplitudes of the QG solution are proportional to ϵA. In the case of $\epsilon A = 0.03$, the dimensional amplitude of the meridional wind disturbance is about 7 m s^{-1}, which is almost the same as that in Sato et al. (1993).

The QG solution shown in Figs. 12a–c represents a clear sinusoidal structure in streamfunction, potential temperature, vertical velocity, and tropopause height. This QG solution is equal to Rivest et al.'s edge wave solution except that the lower boundary is removed here. In contrast, the streamfunction, potential temperature, and vertical velocity anomalies of the QG^{+1} solution shown in Figs. 12d–f are concentrated toward the cyclonic center. The tropopause height of the QG^{+1} solution represents a clear cyclone–anticyclone asymmetry with a deeper cyclone and a flattened anticyclone.

The vertical distributions of KE, PE, and PE/KE of the QG^{+1} solution are shown in Fig. 13. The zero-depth tropopause is located at $z = 0$. The finite-amplitude tropopause height variation resulting from the QG^{+1} wave is neglected. The next-order corrections are computed for $l = 1.8$ instead of $l = 1.4$, as used in Figs. 10–12, because the discontinuity of PE/KE at the tropopause in Fig. 13 is maximized around $l = 1.8$ (i.e., the discontinuity of PE/KE at the tropopause for $l = 1.4$ is about half that for $l = 1.8$).

The solid, dashed, dotted, and dashed-dotted lines in Fig. 13 represent the PE/KE ratio for $\epsilon = 0.1$, 0.3, 0.5, and 0.7, respectively, where $\epsilon A = 0.03$ is fixed. The discontinuity of PE/KE at the tropopause gets larger as

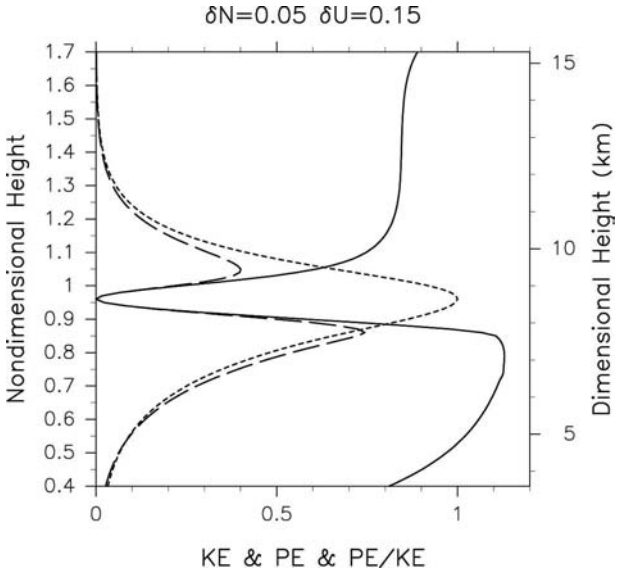

FIG. 11. Vertical distributions of KE (short dashed), PE (long dashed), and PE/KE (solid) of the neutral solution. KE and PE are normalized by the maximum value of KE.

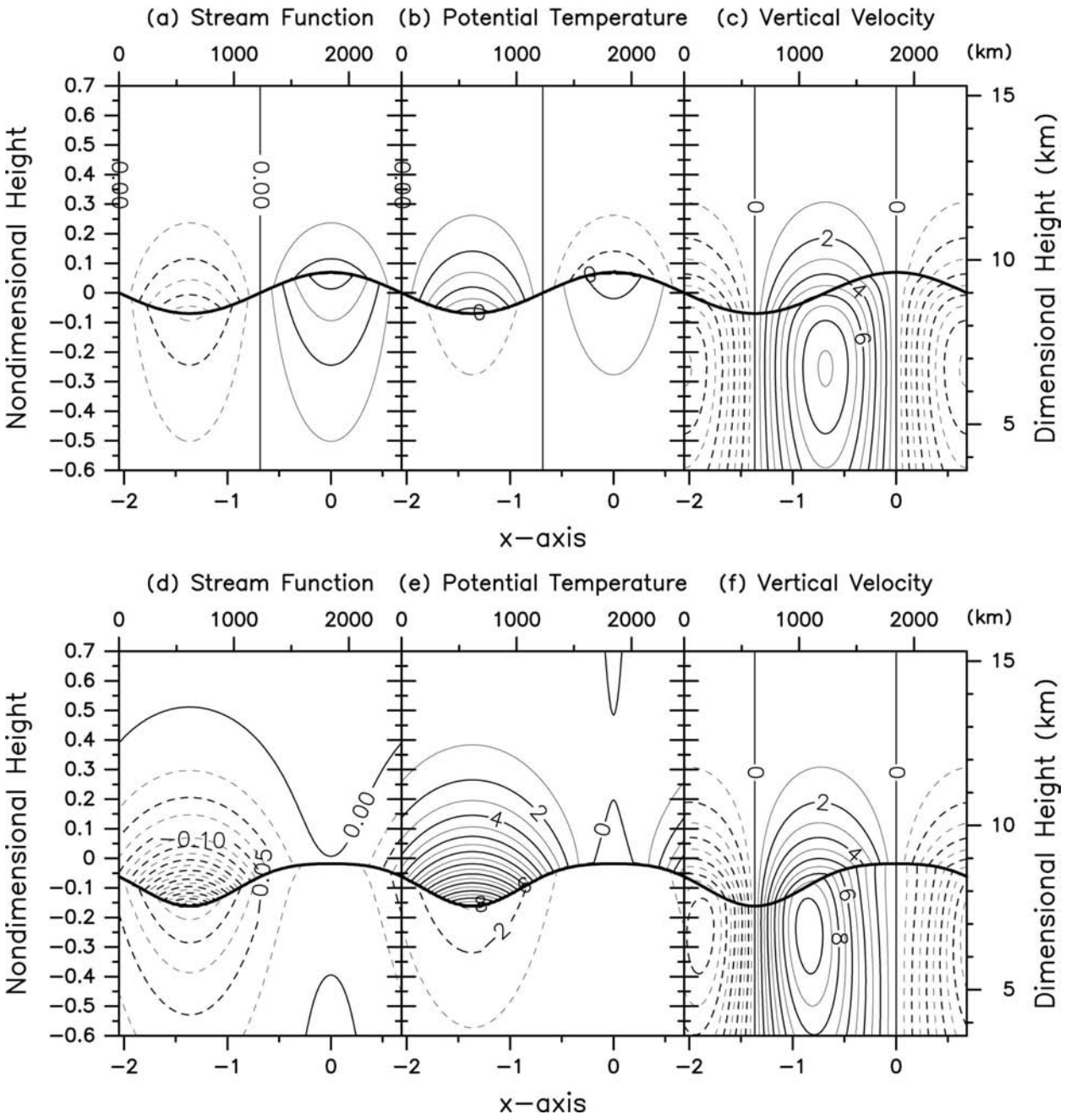

FIG. 12. Zonal cross sections of (a), (d) nondimensional streamfunction, (b), (e) dimensional potential temperature, and (c), (f) vertical velocity of (a)–(c) QG and (d)–(f) QG^{+1} solutions. Contour intervals are 0.025 in (a) and (d), 1 K in (b) and (e), and 1 mm s^{-1} in (c) and (f). Dashed contours represent negative values. Thick solid lines represent the tropopause. Top axis represents a horizontal distance.

the Rossby number increases. Because the zonal wind at the center of the subpolar jet in the SH is 30–40 m s^{-1} as shown in Fig. 5, the Rossby number is expected to be about 0.4 there. Then, the extent of the discontinuity of PE/KE at the tropopause is about 0.15. This fact suggests that the next-order corrections in Rossby number to quasigeostrophic dynamics contribute to the formation of the large asymmetry of the PE/KE maxima between the troposphere and stratosphere.

The cyclone–anticyclone asymmetry of the QG^{+1} solution is largely attributable to nonlinear parts of the next-order corrections (Muraki and Hakim 2001), indi-

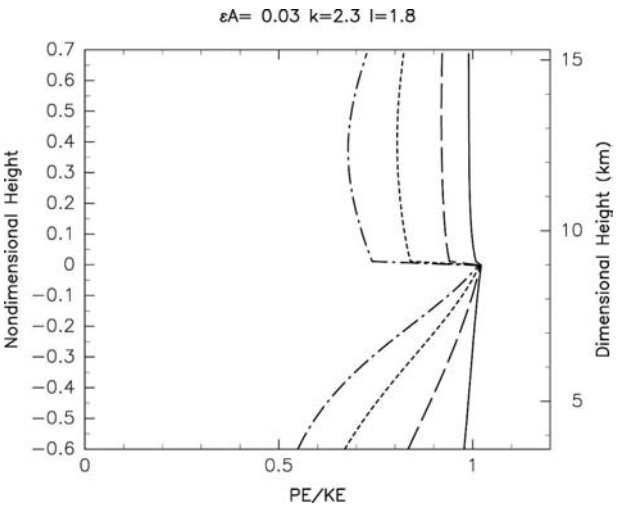

FIG. 13. Vertical distributions of PE/KE with the next-order corrections in Rossby number. Solid, dashed, dotted, and dashed-dotted lines represent the PE/KE for $\epsilon = 0.1$, 0.3, 0.5, and 0.7, respectively.

cating that the nonlinearity of the tropopause disturbances is important even within a wave perspective. On the other hand, the discontinuity of PE/KE at the tropopause largely results from linear parts of the next-order corrections [cf., the third and sixth lines of (B13)]. Thus, it is found that both linear and nonlinear parts of the ageostrophic components given as the next-order corrections have a large effect on the spatial structure of the tropopause disturbances. Note that these next-order corrections do not affect the phase velocity of the edge waves (Muraki and Hakim 2001). Because the Muraki and Hakim model treats the tropopause as a surface, it would be necessary to extend the theory to the case of a finite-depth tropopause for a full comparison. Such an analysis lies outside the scope of this study but would be a good topic for future work.

c. *Tropopause height variations*

To understand the large vertical scale of observed tropopause disturbances, we investigate the effect of tropopause height variations. Figure 14 shows the probability distribution functions of background dynamical tropopause height at 50°S as a function of pressure from January to December. The dynamical tropopause is defined as the -2 PVU ($1\ \text{PVU} = 10^{-6}\ \text{m}^2\ \text{kg}^{-1}\ \text{s}^{-1}$) surface (e.g., Holton et al. 1995). The background dynamical tropopause height varies between 200 and 400 hPa throughout the year. The vertical distributions of KE are computed separately for the cases when the background dynamical tropopause is located at 400–300, 300–250, and 250–200 hPa, and are shown in Fig. 15. It is found that the height of the KE maximum gets slightly lower in most months as the tropopause height gets lower. This means that the vertical distributions of KE shown in Fig. 9 are created by the superposition of KE distributions maximized at different heights, which leads to a broader KE maximum and to a larger apparent vertical scale. Actually, the tropopause disturbance analyzed by Sato et al. (1993) had a vertical scale of about 3 km, which is consistent with the theoretical prediction (Fig. 11) when the tropopause has a finite depth. Thus, it is considered that the large vertical scale found in Fig. 9 is an artifact created by the superposition of tropopause disturbances having a small vertical scale. In the same manner as the KE maximum broadening, the sharpness of the PE minimum at the tropopause in Fig. 9 is reduced compared to the theoretical prediction (Fig. 11), so that the sharpness of the PE/KE minimum at the tropopause in Fig. 9 is also reduced.

5. Summary and concluding remarks

The spatial structure and phase velocity of tropopause disturbances localized around the subpolar jet in the SH were investigated in terms of the edge wave theory of Rivest et al. (1992) using 6-hourly ECMWF Re-Analysis data covering 15 yr (1979–93). The intrinsic phase velocity of tropopause disturbances shows a clear negative correlation with the latitudinal gradient of QGPV at the midlatitude tropopause in terms of daily variability. Their negative correlation is both qualitatively and quantitatively consistent with a theoretical prediction using observed parameters together with Rivest et al.'s edge wave solution. Lag-correlation maps of the tropopause disturbances also support the edge wave theory. On the other hand, the vertical distribution of the PE/KE ratio of the tropopause disturbances shows maxima above and below the tropopause (0.4–0.5 and 1–1.2, respectively) and a minimum around the tropopause (0.1–0.3), in contradiction to the edge wave theory in which the PE/KE ratio should be unity throughout the troposphere and stratosphere.

To explain this inconsistency between observations and edge wave theory for tropopause disturbances, the effect of a finite-depth tropopause on the edge wave solution was examined. With a finite-depth tropopause, the PE/KE ratio is maximized above and below the tropopause and minimized at the tropopause, and the maximum of PE/KE is larger in the troposphere than in the stratosphere. These features are consistent with the observed tropopause disturbances except for a few differences. One difference is the observed large asymmetry of the PE/KE maxima of tropopause disturbances between the troposphere and stratosphere. It was shown that the next-order corrections in Rossby num-

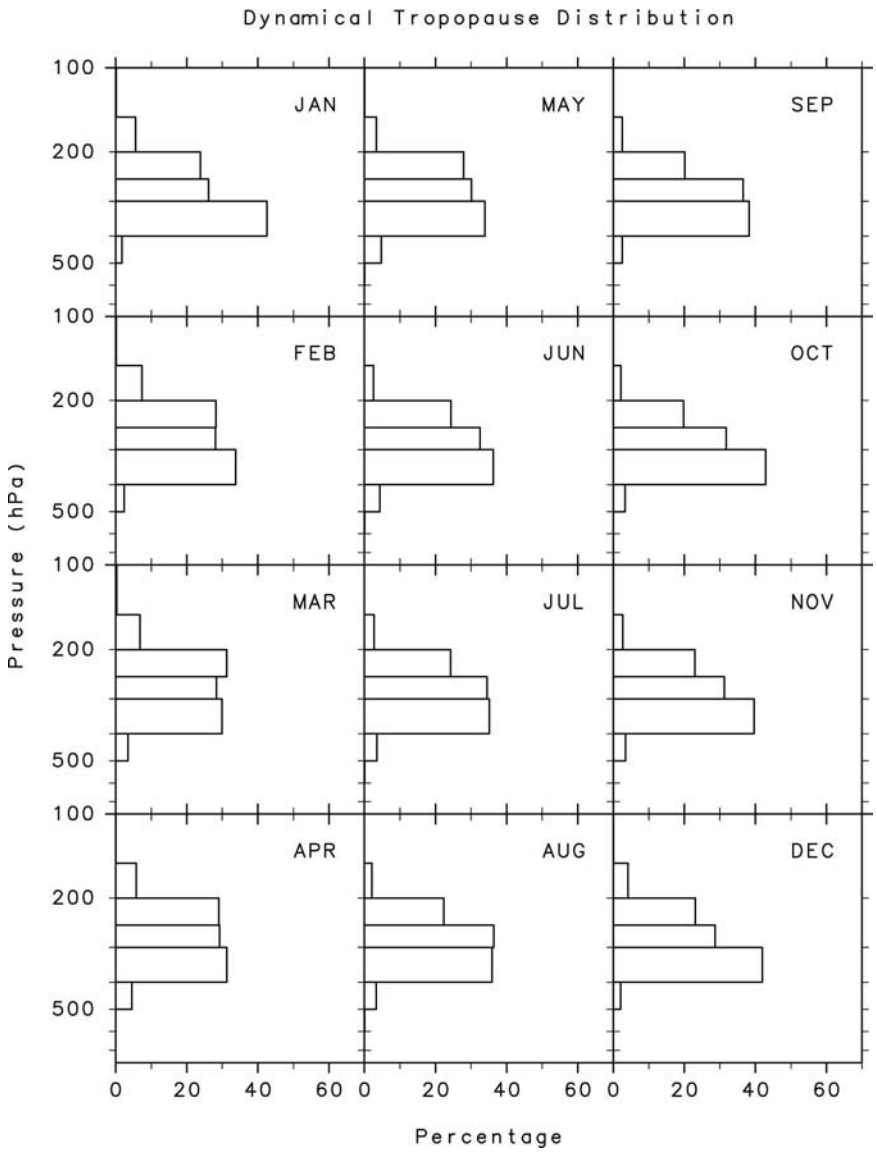

FIG. 14. Probability distribution functions of background dynamical tropopause height at 50°S as a function of pressure in each month from January to December.

ber to quasigeostrophic dynamics could explain the large asymmetry of the PE/KE maxima. Another difference is that the observed tropopause disturbances had a vertical scale larger than the Rossby height, when the vertical scale is determined by the decay of KE away from its maximum in the mean KE distribution. It is argued that this discrepancy primarily results from variations in the background tropopause height, because the tropopause height variation reduces the sharpness of the KE maximum and leads to an overestimate of the vertical scale of the tropopause disturbances. Therefore, it is concluded that most characteristics observed for the vertical structure of tropopause disturbances can be explained by extending the edge wave theory to include the effects of a finite-depth tropopause and ageostrophic dynamics.

One remarkable feature of the tropopause disturbances that is different from synoptic-scale waves is that they are not dominant around the subtropical jet. Nakamura and Shimpo (2004) showed that the subtropical jet in the SH is not associated with large surface baroclinicity. If the baroclinic interactions between tropopause disturbances and surface disturbances are an important amplification mechanism for tropopause disturbances, as suggested by Yamamori and Sato (2002), then the lack of surface disturbances resulting from weak surface baroclinicity might lead to the weak activity of tropopause disturbances around the sub-

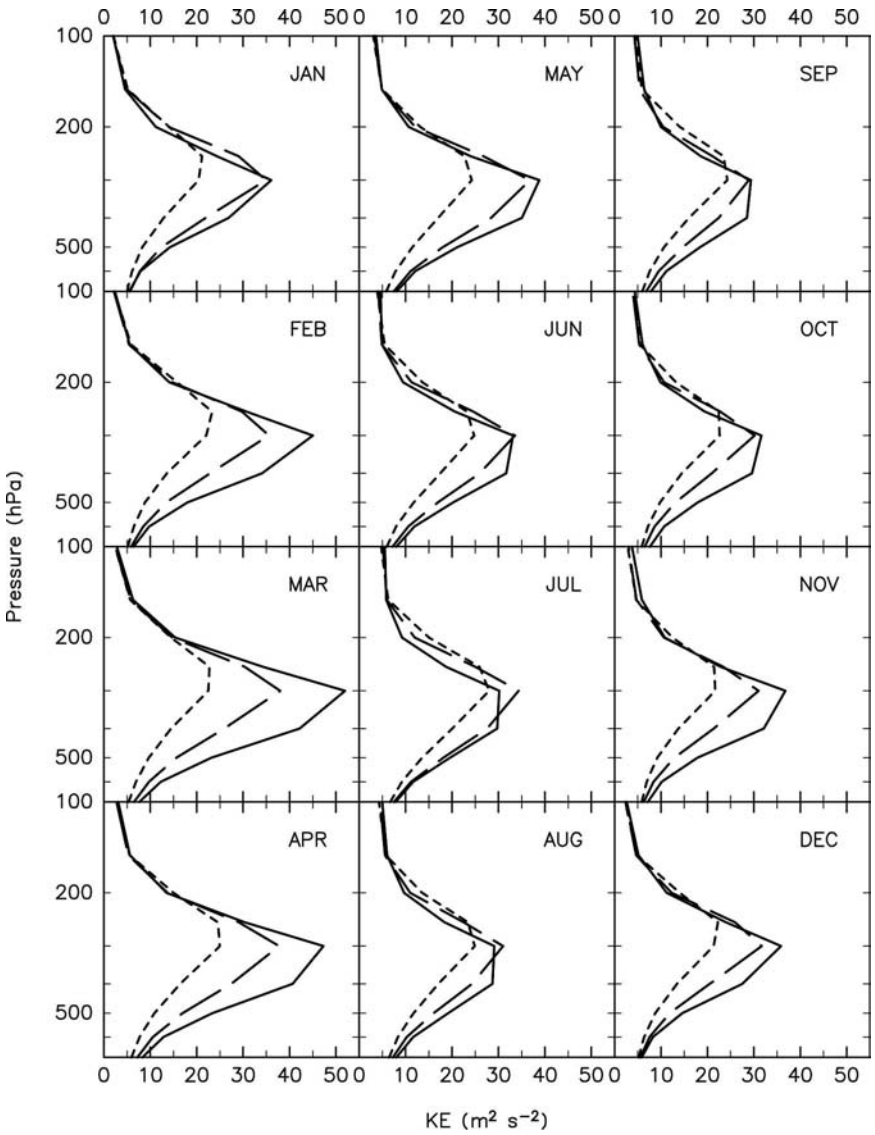

FIG. 15. The same as Fig. 9, but for KE in the case that the background dynamical tropopause is located at 400–300 (solid), 300–250 (long dashed), and 250–200 hPa (short dashed).

tropical jet. Such a formation/amplification mechanism of the tropopause disturbances is still an open question.

Acknowledgments. The authors are grateful to Thomas Birner at the University of Toronto for his helpful comments and suggestions. The authors also acknowledge three anonymous reviewers for their insightful comments. The data used in this paper were provided by ECMWF, and the GFD-DENNOU Library was used for drawing the figures. This research was mainly performed while the first author was visiting the University of Toronto, and is supported by Grant-in-Aid for Scientific Research (B)(2) 12440126 of the Ministry of Education, Culture, Sports, Science and Technology, Japan. The first author (YT) is supported by Research Fellowships of the Japan Society for the Promotion of Science for Young Scientists. The third author (TGS) is supported by the Natural Sciences and Engineering Research Council of Canada, the Canadian Foundation for Climate and Atmospheric Sciences, and the Canadian Space Agency.

APPENDIX A

Basic Equations and the Method of Rivest and Farrell (1992)

Consider perturbations $[q, \psi, u, v, w, \theta]$ (x, y, z, t) to a basic-state flow $[Q, \Psi, U, \Theta]$ (y, z), where $Q + q$ is the

total QGPV, $\Psi + \psi$ the geostrophic streamfunction, $U + u$ the zonal geostrophic wind, υ the meridional geostrophic wind, w the vertical velocity, and $\Theta + \theta$ the potential temperature. The nondimensional quasigeostrophic equations on an f-plane for the basic state are

$$Q_y = -\left[\frac{\partial^2}{\partial y^2} + \frac{1}{\rho}\frac{\partial}{\partial z}\left(\frac{\rho}{N^2}\frac{\partial}{\partial z}\right)\right]U, \tag{A1}$$

$$U = -\frac{\partial \Psi}{\partial y}, \tag{A2}$$

$$\Theta = \frac{\partial \Psi}{\partial z}, \tag{A3}$$

and for the perturbation fields are

$$\left[\frac{\partial}{\partial t} + U\frac{\partial}{\partial x} + J(\psi,)\right]q = -Q_y\frac{\partial \psi}{\partial x}, \tag{A4}$$

$$\left[\frac{\partial}{\partial t} + U\frac{\partial}{\partial x} + J(\psi,)\right]\theta = -N^2 w - \Theta_y\frac{\partial \psi}{\partial x}, \tag{A5}$$

where

$$q = \left[\nabla_H^2 + \frac{1}{\rho}\frac{\partial}{\partial z}\left(\frac{\rho}{N^2}\frac{\partial}{\partial z}\right)\right]\psi, \tag{A6}$$

$$u = -\frac{\partial \psi}{\partial y}, \quad \upsilon = \frac{\partial \psi}{\partial x}, \quad \theta = \frac{\partial \psi}{\partial z},$$

$$J(A, B) = A_x B_y - A_y B_x, \quad \nabla_H^2 = \frac{\partial^2}{\partial x^2} + \frac{\partial^2}{\partial y^2}. \tag{A7}$$

Nondimensionalization of the quasigeostrophic system is based on the disturbance scales $x, y \sim L$, and $z \sim H$, and on the horizontal advective time scale $t \sim L/V$. The other variables are scaled as $U, u, \upsilon \sim V$, $w \sim \epsilon VH/L$, $\Psi, \psi \sim VfL$, $\Theta, \theta \sim VfL\theta_0/gH$, $N \sim N_0$, and $\rho \sim \rho_0$, where $\epsilon \equiv V/fL$ is the Rossby number. Dimensional variables are taken as $f = 10^{-4}\ \mathrm{s}^{-1}$, $L = 900$ km, $H = 9$ km, and $V = 27\ \mathrm{m\ s}^{-1}$, where $\epsilon = 0.3$. We assume a density profile that decays exponentially with height, $\rho = \exp(-sz)$. In the basic state with no meridional shear, the perturbation field is taken as $\psi = \mathrm{Re}[\tilde{\psi}(z)\ \exp ik(x - ct)]\ \sin ly$, where c is a complex phase velocity, and k and l are zonal and meridional wavenumbers, respectively. Then, the perturbation equation (A4) is

$$\left(\frac{\partial}{\partial t} + ikU\right)\tilde{q} = -ikQ_y\tilde{\psi}, \tag{A8}$$

where

$$\tilde{q} = \left[-m^2 - \frac{1}{N^2}\left(s + \frac{1}{N^2}\frac{dN^2}{dz}\right)\frac{\partial}{\partial z} + \frac{1}{N^2}\frac{\partial^2}{\partial z^2}\right]\tilde{\psi}, \tag{A9}$$

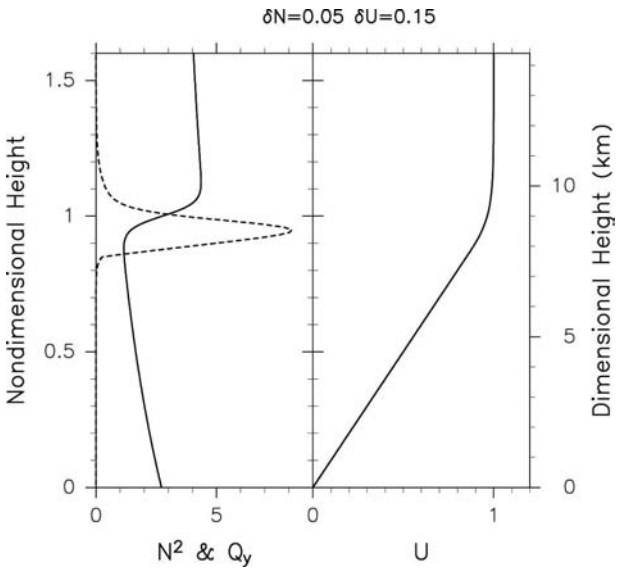

FIG. A1. Vertical distributions of (left) N^2 (solid) and latitudinal gradient of QGPV (dashed) and (right) zonal wind.

and $m \equiv \sqrt{k^2 + l^2}$ is the (nondimensional) horizontal wavenumber. Under the appropriate boundary conditions

$$\left(\frac{\partial}{\partial t} + ikU\right)\frac{\partial \tilde{\psi}}{\partial z} + ik\Theta_y\tilde{\psi} = 0 \quad \text{at} \quad z = 0, \tag{A10}$$

$$\frac{\partial}{\partial t}\left[\frac{\partial \tilde{\psi}}{\partial z} - \left(\frac{s}{2} - \chi_u\right)\tilde{\psi}\right] = -ikU\left[\frac{\partial \tilde{\psi}}{\partial z} - \left(\frac{s}{2} - \chi_u\right)\tilde{\psi}\right] \quad \text{at} \quad z = z_u, \tag{A11}$$

where z_u is the height of the upper boundary, $\chi_u^2 = N_u^2 m^2 + (s^2/4)$, and N_u is N at the upper boundary. The discretized form of (A8) constitutes an eigenvalue problem, where $\tilde{\psi}$ and c correspond to eigenfunctions and eigenvalues, respectively.

The basic state is taken as follows:

$$U(z) = \begin{cases} (z_t - \delta_u) + \delta_u \tanh\left[\dfrac{z - (z_t - \delta_u)}{\delta_u}\right] & z > z_t - \delta_u, \\ z & z < z_t - \delta_u, \end{cases} \tag{A12}$$

$$N^2(z) = \left(\frac{N_S^2 - N_T^2}{2}\right)\left[1 + \tanh\left(\frac{z - z_t}{\delta_N}\right)\right] + N_T^2 e^{-s(z - z_t)}, \tag{A13}$$

where $s = 1$, $z_t = 1$, $\delta_u = 0.15$, $\delta_N = 0.05$, $N_T^2 = 1$, and $N_S^2 = 4.5$. Vertical distributions of basic-state N^2, U, and Q_y are presented in Fig. A1. The vertical distribution of basic-state N^2 reproduces very well the mean N^2

profile computed with ECMWF Re-Analysis data in Birner et al. (2002), although the sharp maximum of N^2 just above the tropopause found in high-resolution radiosonde data (see Fig. 1b of Birner et al. 2002) is not seen in Fig. A1. However, the tropopause disturbances are reproduced well in the ECMWF operational analysis, so the N^2 profile given by (A13) is apparently realistic enough to describe the tropopause disturbances. In Figs. 10 and 11, k and l are 2.3 and 1.4, respectively. More details of the calculation method are given in Rivest and Farrell (1992).

APPENDIX B

Calculation of the Next-Order Corrections in Rossby Number

The primitive variables (u, v, θ) can be represented using three potentials (Φ, F, G) [i.e., Helmholtz decomposition] as

$$\begin{pmatrix} v \\ -u \\ \theta \end{pmatrix} = \begin{pmatrix} \Phi_x - G_z \\ \Phi_y + F_z \\ \Phi_z + G_x - F_y \end{pmatrix}. \tag{B1}$$

Small Rossby number ($\epsilon \ll 1$) and small aspect ratio ($H/L \ll 1$) are assumed. Dimensional variables are the same as in appendix A. After expanding the potentials in Rossby number according to $\Phi = \Phi^0 + \epsilon\Phi^1 + \epsilon^2\Phi^2 + \ldots$, the nondimensional primitive equations at the leading order in Rossby number are equivalent to the quasigeostrophic equations. Thus, under the same basic state as that in Rivest et al. (1992), given by

$$U(z) = \begin{cases} \text{ST:} & 0, \\ \text{TR:} & \Lambda_T z, \end{cases} \qquad N^2(z) = \begin{cases} \text{ST:} & N_S^2, \\ \text{TR:} & N_T^2, \end{cases} \tag{B2}$$

where ST and TR denote the stratosphere and troposphere, respectively, the tropopause is located at $z = 0$, $\Lambda_T = 1$, $N_T^2 = 1$, and $N_S^2 = 4.5$, and the leading-order equations have the same edge wave solution as Rivest et al. (1992) in a moving frame with a zonal phase speed of c,

$$\Phi^0 = \begin{cases} \text{ST:} & A\cos kx\cos ly\exp(-mN_S z), \\ \text{TR:} & A\cos kx\cos ly\exp(mN_T z), \end{cases} \tag{B3}$$

$$c = -\frac{\Lambda_T}{mN_T^2}\left(\frac{1}{N_S} + \frac{1}{N_T}\right)^{-1}, \tag{B4}$$

where A is an amplitude. Note that $F^0 = G^0 = 0$.

From (A1), the QGPV gradient at the zero-depth tropopause is written as

$$\int_{0-}^{0+} Q_y\, dz = -\frac{U_z}{N^2}\bigg|_{0-}^{0+} = \frac{\Lambda_T}{N_T^2}. \tag{B5}$$

Then it is possible to express c as

$$c = -\frac{\displaystyle\int_{0-}^{0+} Q_y\, dz}{m}\left(\frac{1}{N_S} + \frac{1}{N_T}\right)^{-1}. \tag{B6}$$

The next-order corrections of u, v, and θ are given by

$$\begin{aligned} v^1 &= \Phi_x^1 - \frac{1}{N^2}G_z^1, \\ -u^1 &= \Phi_y^1 + \frac{1}{N^2}F_z^1 + \sigma\Phi_z^0 \\ \theta^1 &= \Phi_z^1 + G_x^1 - F_y^1, \end{aligned} \tag{B7}$$

where $\sigma = \Lambda_T/(N_S^2 - N_T^2)$. The next-order corrections to the potentials are

$$\begin{aligned} \Phi^1 &= \frac{1}{2N^2}(\Phi_z^0)^2 - (U_z + \sigma N^2)z\Phi_y^0 + U_z\int \Phi_y^0\, dz + \tilde{\Phi}_{\text{nl}}^1 \\ F^1 &= \Phi_y^0\Phi_z^0 + U_z N^2 z\int \Phi_{xx}^0\, dz + c\Phi_z^0 + U_z\Phi^0, \\ G^1 &= -\Phi_x^0\Phi_z^0 + U_z N^2 z\int \Phi_{xy}^0\, dz. \end{aligned} \tag{B8}$$

The nonlinear part $\tilde{\Phi}_{\text{nl}}^1$ is given by

$$\tilde{\Phi}_{\text{nl}}^1 = \begin{cases} \text{ST:} & \sum A_{KL}\cos Kx\cos Ly\exp(-MN_S z), \\ \text{TR:} & \sum B_{KL}\cos Kx\cos Ly\exp(MN_T z), \end{cases} \tag{B9}$$

where $M = \sqrt{K^2 + L^2}$ and the sum is over the wavenumbers

$$(K, L; M) = (0, 0; 0), (2k, 0; 2k), (0, 2l; 2l), (2k, 2l; 2m). \tag{B10}$$

The coefficients are

$$A_{KL} = \left[-\left(\frac{M}{N_T} + \frac{\Lambda_T}{cN_T^2} + \frac{\sigma}{c}\right)\mathcal{F}_1 + \mathcal{F}_2\right]\cdot\mathcal{D}^{-1}, \tag{B11}$$

$$\begin{aligned} B_{KL} &= \left[\left(\frac{M}{N_S} - \frac{\sigma}{c}\right)\mathcal{F}_1 + \mathcal{F}_2\right]\cdot\mathcal{D}^{-1}, \\ \mathcal{D} &= -\frac{\Lambda_T}{cN_T^2} - M\left(\frac{1}{N_S} + \frac{1}{N_T}\right), \\ \mathcal{F}_1 &= \frac{N_S + N_T}{8(N_S - N_T)}m^2A^2, \quad \mathcal{F}_2 = \frac{-C_1M^2 + C_2}{4}A^2, \\ C_1 &= \frac{\Lambda_T}{2cN_T^2}, \quad C_2 = \frac{\sigma C_1}{c^2}\left(\frac{\Lambda_T}{N_T^2} + 2\sigma\right). \end{aligned} \tag{B12}$$

By substituting (B8) into (B7), the next-order corrections in u, v, and θ can be obtained. Then, the PE/KE ratio is given by

$$
\frac{\mathrm{PE}}{\mathrm{KE}} = \left\{
\begin{aligned}
&\text{ST:}\quad \left\langle 1+\epsilon^2\left\{\left[\frac{13m^4+2(2k^2+m^2)^2+2(2l^2+m^2)^2}{16}A^2+3m^2A_{22}+\frac{4A_{22}^2}{A^2}\right]\exp(-2mN_Sz)\right.\right.\\
&\quad+\frac{8}{m^2A^2}[k^2A_{20}^2\exp(-4kN_Sz)+l^2A_{02}^2\exp(-4lN_Sz)]\exp(2mN_Sz)\\
&\quad+\frac{l^2[\sigma N_S^2(1-mN_Sz)-mN_Sc]^2}{m^2N_S^2}\\
&\quad\left.\left.+\frac{2}{m}[k(2k^2+m^2)A_{20}\exp(-2kN_Sz)+l(2l^2+m^2)A_{02}\exp(-2lN_Sz)]\right\}\right\rangle\\
&\quad\times\left\langle 1+\epsilon^2\left\{\left(\frac{27}{16}m^4A^2+3m^2A_{22}+\frac{4A_{22}^2}{A^2}\right)\exp(-2mN_Sz)\right.\right.\\
&\quad+\frac{8}{m^2A^2}[k^2A_{20}^2\exp(-4kN_Sz)+l^2A_{02}^2\exp(-4lN_Sz)]\exp(2mN_Sz)\\
&\quad+\frac{k^2l^2\sigma^2N_S^4z^2+(-l^2\sigma N_S^2z-cm^2+mN_S\sigma)^2}{m^2}\\
&\quad\left.\left.+6[k^2A_{20}\exp(-2kN_Sz)+l^2A_{02}\exp(-2lN_Sz)]\right\}\right\rangle^{-1},\\
&\text{TR:}\quad \left\langle 1+\epsilon^2\left\{\left[\frac{13m^4+2(2k^2+m^2)^2+2(2l^2+m^2)^2}{16}A^2+3m^2B_{22}+\frac{4B_{22}^2}{A^2}\right]\exp(2mN_Tz)\right.\right.\\
&\quad+\frac{8}{m^2A^2}[k^2B_{20}^2\exp(4kN_Tz)+l^2B_{02}^2\exp(4lN_Tz)]\exp(-2mN_Tz)\\
&\quad+\frac{l^2[(\Lambda_T+\sigma N_T^2)(1+mN_Tz)+mN_Tc]^2}{m^2N_T^2}\\
&\quad\left.\left.+\frac{2}{m}[k(2k^2+m^2)B_{20}\exp(2kN_Tz)+l(2l^2+m^2)B_{02}\exp(2lN_Tz)]\right\}\right\rangle\\
&\quad\times\left\langle 1+\epsilon^2\left\{\left(\frac{27}{16}m^4A^2+3m^2B_{22}+\frac{4B_{22}^2}{A^2}\right)\exp(2mN_Tz)\right.\right.\\
&\quad+\frac{8}{m^2A^2}[k^2B_{20}^2\exp(4kN_Tz)+l^2B_{02}^2\exp(4lN_Tz)]\exp(-2mN_Tz)\\
&\quad+\frac{k^2l^2(2\Lambda_T+\sigma N_T^2)^2z^2+\{[k^2\Lambda_T-l^2(\Lambda_T+\sigma N_T^2)]z-cm^2-mN_T\sigma\}^2}{m^2}\\
&\quad\left.\left.+6[k^2B_{20}\exp(2kN_Tz)+l^2B_{02}\exp(2lN_Tz)]\right\}\right\rangle^{-1}.
\end{aligned}
\right. \tag{B13}
$$

In Fig. 13, $A = 1$, $k = 2.3$, and $l = 1.8$. More details of the derivation are given in Muraki and Hakim (2001).

REFERENCES

Andrews, D. G., J. R. Holton, and C. B. Leovy, 1987: *Middle Atmosphere Dynamics.* Academic Press, 489 pp.

Berbery, E. H., and C. S. Vera, 1996: Characteristics of the Southern Hemisphere winter storm track with filtered and unfiltered data. *J. Atmos. Sci.,* **53,** 468–481.

Birner, T., A. Dörnbrack, and U. Schumann, 2002: How sharp is the tropopause at midlatitudes? *Geophys. Res. Lett.,* **29,** 1700, doi:10.1029/2002GL015142.

Cunningham, P., and D. Keyser, 2000: Analytical and numerical

modelling of jet streaks: Barotropic dynamics. *Quart. J. Roy. Meteor. Soc.,* **126,** 3187–3217.

——, and ——, 2004: Dynamics of jet streaks in a stratified quasi-geostrophic atmosphere: Steady-state representations. *Quart. J. Roy. Meteor. Soc.,* **130,** 1579–1609.

Farrell, B. F., 1982: The initial growth of disturbances in a baroclinic flow. *J. Atmos. Sci.,* **39,** 1663–1686.

Gibson, J. K., P. Kållberg, S. Uppala, A. Hernandez, A. Nomura, and E. Serrano, 1997: ERA description. ECMWF Re-Analysis (ERA) Project Report Series 1, 72 pp.

Hakim, G. J., 2000: Climatology of coherent structures on the extratropical tropopause. *Mon. Wea. Rev.,* **128,** 385–406.

——, and A. K. Canavan, 2005: Observed cyclone–anticyclone tropopause vortex asymmetries. *J. Atmos. Sci.,* **62,** 231–240.

Hirota, I., K. Yamada, and K. Sato, 1995: Medium-scale travelling waves over the north Atlantic. *J. Meteor. Soc. Japan,* **73,** 1175–1179.

Holton, J. R., P. Haynes, M. E. McIntyre, A. R. Douglass, R. B. Rood, and L. Pfister, 1995: Stratosphere-troposphere exchange. *Rev. Geophys.,* **33,** 403–439.

Horinouchi, T., and Coauthors, 2003: Tropical cumulus convection and upward-propagating waves in middle-atmospheric GCMs. *J. Atmos. Sci.,* **60,** 2765–2782.

Hoskins, B. J., M. E. McIntyre, and A. W. Robertson, 1985: On the use and significance of isentropic potential vorticity maps. *Quart. J. Roy. Meteor. Soc.,* **111,** 877–946.

Juckes, M., 1994: Quasigeostrophic dynamics of the tropopause. *J. Atmos. Sci.,* **51,** 2756–2768.

Lefevre, R. J., and J. W. Nielsen-Gammon, 1995: An objective climatology of mobile troughs in the northern hemisphere. *Tellus,* **47A,** 638–655.

Muraki, D. J., and G. J. Hakim, 2001: Balanced asymmetries of waves on the tropopause. *J. Atmos. Sci.,* **58,** 237–252.

——, C. Snyder, and R. Rotunno, 1999: The next-order corrections to quasigeostrophic theory. *J. Atmos. Sci.,* **56,** 1547–1560.

Nakamura, H., and A. Shimpo, 2004: Seasonal variations in the Southern Hemisphere storm tracks and jet streams as revealed in a reanalysis dataset. *J. Climate,* **17,** 1828–1844.

Petterssen, S., and S. J. Smebye, 1971: On the development of extratropical cyclones. *Quart. J. Roy. Meteor. Soc.,* **97,** 457–482.

Pyle, M. E., D. Keyser, and L. F. Bosart, 2004: A diagnostic study of jet streaks: Kinematic signatures and relationship to coherent tropopause disturbances. *Mon. Wea. Rev.,* **132,** 297–319.

Rivest, C., and B. F. Farrell, 1992: Upper-tropospheric synoptic-scale waves. Part II: Maintenance and excitation of quasi modes. *J. Atmos. Sci.,* **49,** 2120–2138.

——, C. A. Davis, and B. F. Farrell, 1992: Upper-tropospheric synoptic-scale waves. Part I: Maintenance as Eady normal modes. *J. Atmos. Sci.,* **49,** 2108–2119.

Sanders, F., 1988: Life history of mobile troughs in the upper westerlies. *Mon. Wea. Rev.,* **116,** 2629–2648.

Sato, K., H. Eito, and I. Hirota, 1993: Medium-scale travelling waves in the extra-tropical upper troposphere. *J. Meteor. Soc. Japan,* **71,** 427–436.

——, K. Yamada, and I. Hirota, 2000: Global characteristics of medium-scale tropopausal waves observed in ECMWF operational data. *Mon. Wea. Rev.,* **128,** 3808–3823.

Tomikawa, Y., and K. Sato, 2003: Trapped waves in the edge region of stratospheric polar vortices. *J. Geophys. Res.,* **108,** 4047, doi:10.1029/2002JD002579.

Wallace, J. M., G.-H. Lim, and M. L. Blackmon, 1988: Relationship between cyclone tracks, anticyclone tracks and baroclinic waveguides. *J. Atmos. Sci.,* **45,** 439–462.

Yamamori, M., and K. Sato, 2002: An amplification mechanism of medium-scale tropopausal waves. *Mon. Wea. Rev.,* **130,** 1455–1467.

——, ——, and I. Hirota, 1997: A study on seasonal variation of upper tropospheric medium-scale waves over east Asia based on regional climate model data. *J. Meteor. Soc. Japan,* **75,** 13–22.